Dynamics of exciton recombination in strong magnetic fields in ultrathin GaAs/AlAs quantum wells with indirect band gap and type-II band alignment

T. S. Shamirzaev,[1,2,3] J. Debus,[4] D. R. Yakovlev,[4,5] M. M. Glazov,[5] E. L. Ivchenko,[5] and M. Bayer[4,5]

[1]*Rzhanov Institute of Semiconductor Physics, Siberian Branch of the Russian Academy of Sciences, 630090 Novosibirsk, Russia*

[2]*Novosibirsk State University, 630090 Novosibirsk, Russia*

[3]*Ural Federal University, 620002 Yekaterinburg, Russia*

[4]*Experimentelle Physik 2, Technische Universität Dortmund, 44227 Dortmund, Germany*

[5]*Ioffe Institute, Russian Academy of Sciences, 194021 St. Petersburg, Russia*

(Received 14 May 2016; published 8 July 2016)

The exciton recombination dynamics is studied experimentally and theoretically in two-monolayer-thick GaAs/AlAs quantum wells characterized by an indirect band gap and a type-II band alignment. At cryogenic temperatures, the lifetimes of the excitons that are indirect both in real and $\boldsymbol{k}$ space are in the millisecond range. The exciton recombination time and the photoluminescence (PL) intensity are strongly dependent on strength and orientation of an applied magnetic field. In contrast to the very weak influence of an in-plane field, at 2 K temperature a field applied parallel to the growth axis drastically slows down the recombination and reduces the PL intensity. With increasing temperature the magnetic field effects on PL intensity and decay time are vanishing. The experimental data are well described by a model for the exciton dynamics that takes into account the magnetic-field-induced redistribution of the indirect excitons between their bright and dark states. It allows us to evaluate the lower bound of the heavy-hole longitudinal g factor of 2.5, the radiative recombination time for the bright excitons of 0.34 ms, and the nonradiative recombination time of the bright and dark excitons of 8.5 ms.

DOI: 10.1103/PhysRevB.94.045411

I. INTRODUCTION

Excitons in low-dimensional semiconductor systems determine the optical properties of nano-sized materials and are interesting from the viewpoint of both basic physics and potential applications [1,2]. One of the fundamental parameters of low-dimensional excitons is their recombination time that can be controlled by the band gap type, direct or indirect, and the band alignment in heterostructures; see Fig. 1. Unlike in structures with a type-I band alignment, where electrons and holes are confined in the same layer, Figs. 1(c) and 1(d), in structures with a type-II band alignment the electrons and holes are separated in real space and confined in neighboring layers of the heterostructure, Figs. 1(e) and 1(f). Also in momentum space either overlap or separation of the carriers is possible. Thus, four different scenarios of band alignment can be realized in general.

The typical recombination times of excitons in direct band-gap heterostructures of type I, such as (In,Ga)As/GaAs or GaAs/(Al,Ga)As quantum wells (QWs), are on the order of a fraction to several nanoseconds [3]. They can be increased to hundreds of nanoseconds in direct band gap heterostructures of type II [4], e.g., GaSb/GaAs; see Fig. 1(e). On the other hand, momentum separation of electrons and holes in type-I indirect band gap heterostructures such as (In,Al)As/AlAs, Fig. 1(d), allows one to increase the exciton lifetime up to hundreds of microseconds [5]. An additional increase in the lifetime is achieved by spatial separation of charge carriers in indirect band-gap heterostructures of type II, Fig. 1(f), such as GaAs/AlAs QWs and superlattices [6]. These long exciton lifetimes make the latter structures highly interesting for studying the exciton spin dynamics and, in particular, seeking for long electron spin relaxation times which, according to theoretical estimations, may reach milliseconds [7,8].

Up to now, only a few works were devoted to exciton spin relaxation in GaAs/AlAs type-II heterostructures where the electron ground states are located at the X_z valley of the conduction band [9–14]. In these studies the structures were placed in an external magnetic field, which may affect the exciton spin relaxation and, as a result, control the recombination of the excitons due to their redistribution between bright and dark states [15]. However, this effect has been scarcely studied so far.

In this paper, we investigate the effects of a magnetic field on the exciton recombination dynamics in ultrathin GaAs/AlAs QWs with indirect band gap and type-II band alignment. The exciton photoluminescence (PL) shows an unusual behavior. In the Voigt geometry the magnetic field does not affect the PL, whereas in the Faraday geometry increasing the magnetic field results in a strong suppression of the PL intensity combined with an increase of the exciton recombination time. These experimental data are explained in the framework of a theoretical model taking into account the exciton distribution over the bright and dark states.

The paper is organized as follows. In Sec. II the samples studied and the experimental techniques are described. In Sec. III we present the experimental data on the exciton dynamics obtained in external magnetic field by time-integrated and time-resolved PL. The theoretical model describing the exciton dynamics in the ultrathin GaAs/AlAs QWs is developed in Sec. IV. In Sec. V we discuss the data in relation to this model.

II. EXPERIMENTAL DETAILS

The GaAs/AlAs QW sample studied in this work was grown by molecular-beam epitaxy on a semi-insulating (001)-oriented GaAs substrate in a Riber Compact system. The

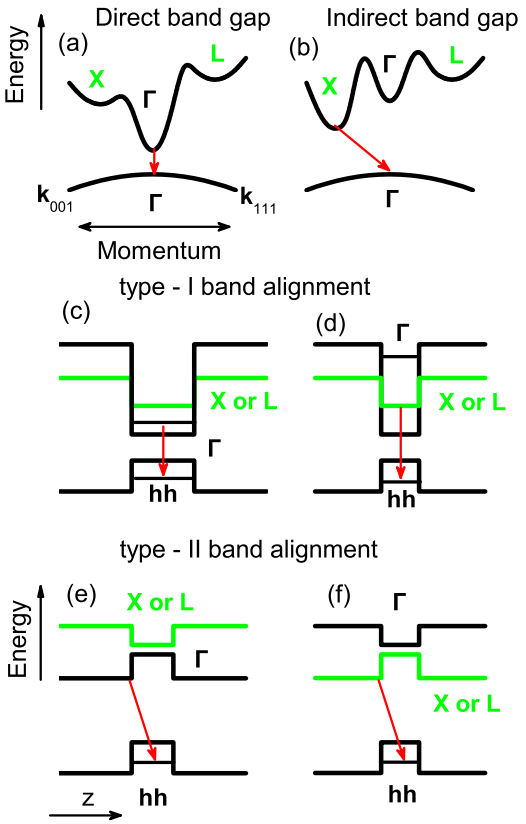

FIG. 1. Schematic band diagrams of heterostructures. In the quasimomentum space: (a) direct and (b) indirect band gaps. In the real space: (c) type-I direct band gap, (d) type-I indirect band gap, (e) type-II direct band gap, (f) type-II indirect band gap. Red arrows mark optical transitions of the exciton to the system ground state.

sample consists of a GaAs QW layer embedded between 50-nm-thick layers of AlAs grown on top of a 200-nm-thick GaAs buffer layer [16]. The substrate temperature during growth was 600 °C. The GaAs QW layer was deposited with a nominal thickness of two monolayers. A 20-nm-thick GaAs cap layer protects the top AlAs layer against oxidation. Further growth details are given in Ref. [5]. The GaAs/AlAs QW has a type-II band alignment with the lowest conduction-band states at the X_{xy} minima of the AlAs conduction band [5,6,9], which leads to the band structure scheme of Fig. 1(f).

The sample was placed in a split-coil magnet cryostat and exposed to magnetic fields up to $B = 10$ T. The angle θ between the magnetic field direction and the QW growth axis (z axis) was varied between 0° (Faraday geometry) and 90° (Voigt geometry). The temperature was varied from $T = 1.8$ K up to 16 K. The PL was excited by the third harmonic of a Q-switched Nd:YVO_4 laser (3.49 eV) with a pulse duration of 5 ns. The pulse energy density was kept below 100 nJ/cm^2 and the pulse-repetition frequency was varied from 20 Hz up to 1 kHz [17]. The emitted light was dispersed by a 0.5-m monochromator. For the time-integrated measurements the photoluminescence was detected by a liquid-nitrogen-cooled charge-coupled-device (CCD) camera and for the time-resolved measurements a GaAs photomultiplier combined with a time-correlated photon-counting module was used. In order to monitor the PL decay in a wide temporal range of

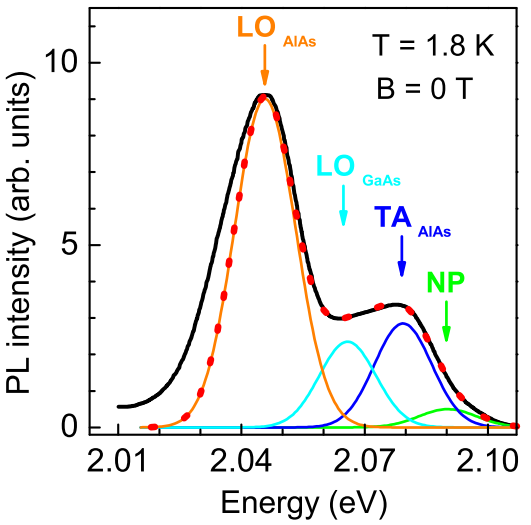

FIG. 2. Time-integrated PL spectrum of the ultrathin GaAs/AlAs QW (black line) fitted with four Gaussian lines corresponding to the exciton recombination channels with and without involvement of phonons. Green, blue, cyan, and orange solid lines are the no-phonon, TA_{AlAs}, LO_{GaAs}, and LO_{AlAs} phonon lines, respectively. Red dotted line is a fitted spectrum composed of the four lines.

up to 30 ms, the time resolution of the detection system (i.e., the binning range of the photon counting events) was varied between 3.2 ns and 6.4 μs.

III. EXPERIMENTAL RESULTS

A. Time-integrated photoluminescence

A time-integrated photoluminescence spectrum of the ultrathin GaAs/AlAs QW is shown in Fig. 2 by the black line. The spectrum is contributed by several emission processes; it contains a no-phonon (NP) line and several lines of phonon-assisted recombination involving optical and acoustic phonons from GaAs and AlAs. The replicas associated with the transverse acoustic (TA) phonons of AlAs (12 meV) and the longitudinal optical (LO) phonons of GaAs (30 meV) and AlAs (48 meV), all at the X point of the Brillouin zone [18], are clearly seen. The lines are broadened due to the roughness of the QW interface [5]. An exemplary fitting of the PL spectrum with four contributing Gaussian curves, each with the same width of 19 meV, is shown in Fig. 2 by the red dotted line. The energy positions of the phonon lines are shifted from the position of the NP line at 2.09 eV by the corresponding phonon energies. The deviation of the fitted spectrum from the experimental one in the low-energy region may result from two-phonon transitions that are not taken into account in the fitting procedure.

It is documented in Fig. 3 that the PL intensity (I_{PL}) depends on orientation and strength of the applied magnetic field. In the Voigt geometry the magnetic field does not affect the photoluminescence, while in the Faraday geometry the PL intensity decreases drastically with increasing magnetic field strength. Application of the magnetic field results in polarization of the emission. At $B = 5$ T and $T = 2$ K a linear polarization degree of 20% is achieved in the Voigt geometry [Fig. 3(c)] and a circular polarization degree of 50% in the Faraday one

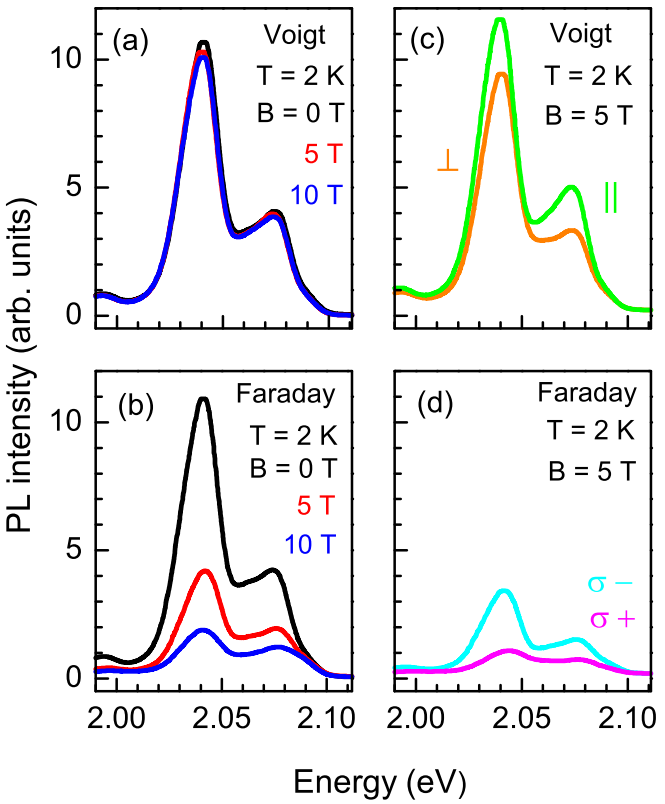

FIG. 3. Time-integrated PL spectra of the ultrathin GaAs/AlAs QW measured at different magnetic fields: (a) Voigt geometry, (b) Faraday geometry. The PL spectra at $B = 5$ T were taken in different polarizations: (c) linear polarization parallel and perpendicular to the magnetic field direction in the Voigt geometry, (d) left- and right-circular polarization in the Faraday geometry.

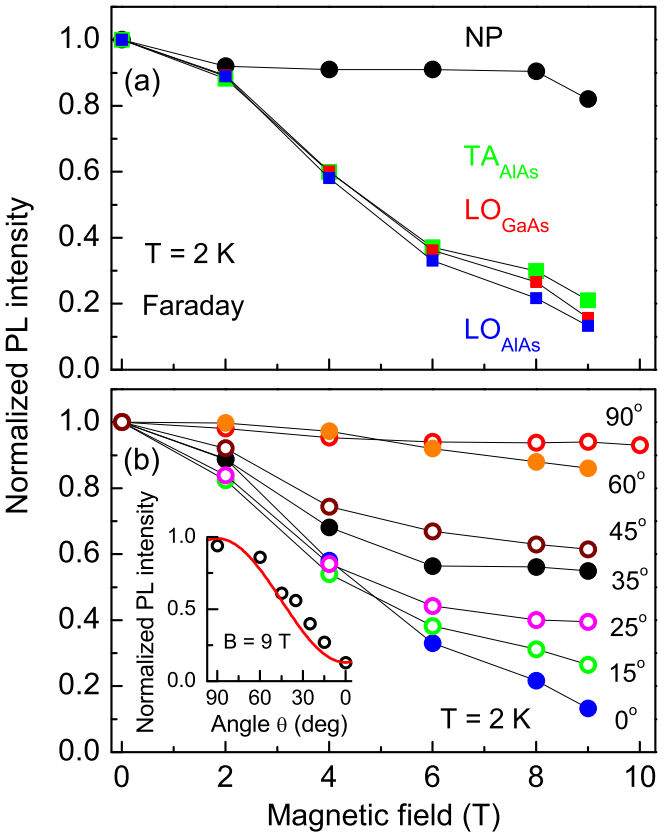

FIG. 4. (a) Normalized PL intensity of the NP line and the phonon-assisted lines as function of magnetic field applied in the Faraday geometry. (b) Normalized intensity of the integrated PL as a function of magnetic field strength measured for various angles θ between the magnetic field direction and the QW growth axis. Black lines in both panels are guides to the eye. Inset shows change of the integrated PL intensity with angle θ at $B = 9$ T. Red line shows $\sin^2\theta$ dependence.

[Fig. 3(d)]. However, the polarization properties and related carrier spin dynamics are beyond the scope of this study.

Let us have a closer look at the magnetic field effect on the no-phonon and phonon-assisted lines. From fitting the PL spectra in magnetic field with the four Gaussian lines, see the example in Fig. 2, the time-integrated intensities of these lines as a function of longitudinal magnetic field are obtained as shown in Fig. 4(a). Interestingly the NP line and the phonon-assisted lines show very different behavior. The intensity of the NP line is about constant; it decreases only by about 10% up to $B = 9$ T. By contrast, the intensities of the phonon-assisted lines are reduced by a factor of 5.

The identification of the origin of the NP line has not been fully completed so far. We suggest that it is dominated by trions, i.e., charged excitons, formed from photogenerated electron-hole pairs and residual carriers. The presence of the third carrier in the trion complex relaxes the momentum conservation law and opens up a recombination channel which does not require phonon involvement. The trion origin of the NP line is also consistent with a weak magnetic field effect on its PL intensity as compared with the phonon-assisted lines. The contribution of the NP line to the integrated intensity of the PL band does not exceed 10% in the highest longitudinal magnetic field of 10 T, and it becomes much smaller in lower fields. Therefore, we exclude the NP line from the further analysis and will focus on the properties of the phonon-assisted lines.

The magnetic-field-induced changes of the intensity of the phonon-assisted lines depend strongly on the experimental geometry. They are maximal in the Faraday geometry, and are absent in the Voigt geometry. In Fig. 4(b) it is shown how the PL intensity decreases when rotating the magnetic field from the Voigt towards the Faraday geometry. Here θ is the angle between the magnetic field direction and the QW growth axis. The dependence of the PL intensity on θ at $B = 9$ T is given in the inset of Fig. 4(b).

Photoluminescence spectra of the GaAs/AlAs QW measured at $B = 0$ T for different temperatures are shown in Fig. 5(a). At zero magnetic field, the PL intensity integrated over the whole spectrum monotonically decreases by about one order of magnitude with temperature increase from 2 K up to 16 K, as one can see in Fig. 5(c). This decrease is related to nonradiative centers at the heterointerfaces, which capture excitons more efficiently at elevated temperatures because the exciton diffusion length increases with increasing temperature [6,19]. Simultaneously, the PL band demonstrates a small low-energy shift $\Delta E = 2$ meV.

In the Voigt geometry an increase of the magnetic field up to 10 T has no effect on the temperature dependence of the PL intensity (not shown). Under application of the field

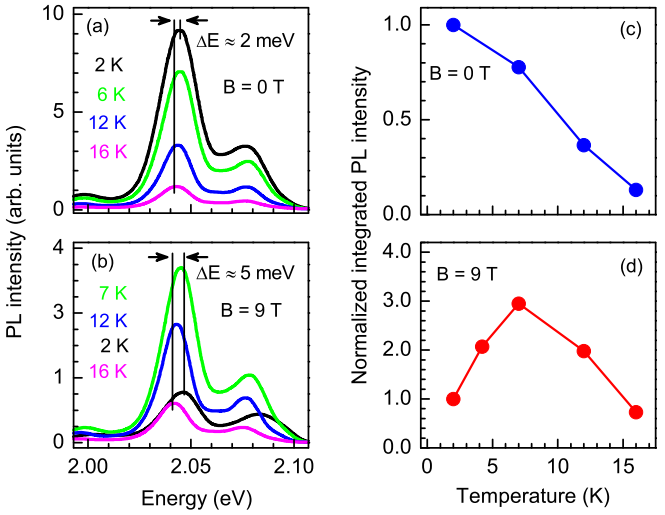

FIG. 5. PL spectra of the GaAs/AlAs QW measured in Faraday geometry at different temperatures: (a) $B = 0$ T, (b) $B = 9$ T. Normalized intensity of the integrated PL as a function of temperature: (c) $B = 0$ T, (d) $B = 9$ T.

in the Faraday configuration, the temperature dependence changes drastically. The PL intensity increases by a factor of 3 with increasing temperature from 2 K up to 7 K; see Fig. 5(b). It is surprising, that such small changes in temperature result in an almost complete recovery of the PL intensity that was suppressed by the longitudinal magnetic field. A further temperature increase up to 16 K results in a monotonic decrease of the PL intensity; details of the temperature dependence are given in Fig. 5(d).

Also, the temperature increase from 2 K to 16 K leads to a redshift of the PL peak by $\Delta E = 2$ meV at zero magnetic field and by $\Delta E = 5$ meV in longitudinal magnetic field of 9 T. This shift exceeds the temperature variation of the band gap and, obviously, has a purely dynamical origin. For $T \to 0$, the PL is contributed by localized excitons occupying isolated states for which the hopping time down to the nearest lower-energy localization sites exceeds the recombination time. At increased but still low temperature, an exciton trapped by such a "potential pocket" gets the opportunity of hopping up to the nearest higher-energy state and then down to a deeper-energy site [15]. The dependence $\Delta E(B)$ could be related to a shrinkage of the exciton envelope function in longitudinal magnetic field.

B. Time-resolved photoluminescence

The photoluminescence dynamics measured for the NP, TA_{AlAs}, and LO_{AlAs} lines are shown in Fig. 6. At $T = 2$ K and $B = 0$ T the recombination has two distinct stages: (i) a fast nonexponential decrease during the first microsecond after the excitation pulse shown in Fig. 6(a), followed by (ii) an exponential decay with the same for all lines decay time $\tau_{PL} = 0.65$ ms [Fig. 6(b)]. Since more than 95% of the intensity in the time-integrated spectra is collected within the time range exceeding one microsecond, we focus in our analysis on the long-term dynamics. All lines show similar changes in their dynamics with varying temperature, magnetic field

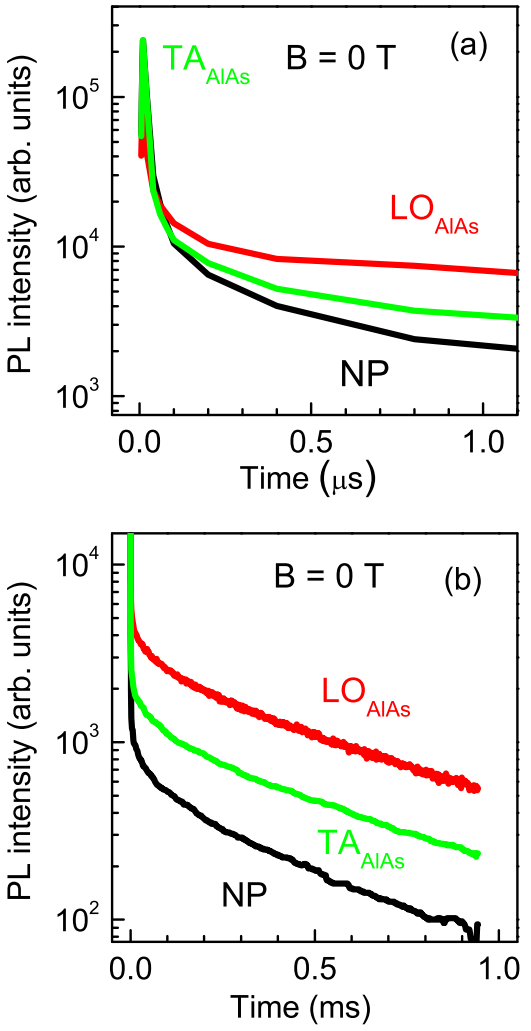

FIG. 6. PL decays of the NP (black), TA_{AlAs} (green), and LO_{AlAs} (red) components measured at $B = 0$ T and $T = 2$ K. (a) Initial time range up to 1 μs. (b) Time range up to 1 ms after the excitation pulse. Note that here the initial decay is not shown.

strength, and sample orientation. Therefore, we present and discuss below the typical behavior of the LO_{AlAs} line that is the strongest in intensity.

The magnetic field applied in the Voigt geometry does not affect the PL dynamics as one can see in the inset of Fig. 7(a), where the dynamics of the LO_{AlAs} line measured at $B = 0$ T coincides with that for $B = 10$ T in the Voigt geometry. On the contrary, strong changes are observed in the Faraday geometry; see Fig. 7(a). Here, the decay time of the long-term component increases from 0.65 ms to 8 ms with increasing magnetic field from 0 up to 10 T. The decay times are depicted in Fig. 8. In the tilted-field configuration with $\theta = 45^\circ$ the decay times are between those values for the Faraday and Voigt geometries; see Fig. 7(b).

The temperature increase leads to a recovery of the fast PL intensity decay for longitudinal and tilted magnetic field. One can see in Fig. 8 that already at $T = 10$ K the magnetic field dependence of τ_{PL} is nearly absent, while it is strong at 2 K.

As noted above, the spin dynamics is not in the focus of this paper. However, to provide an interpretation of the recombination dynamics and its prominent magnetic field

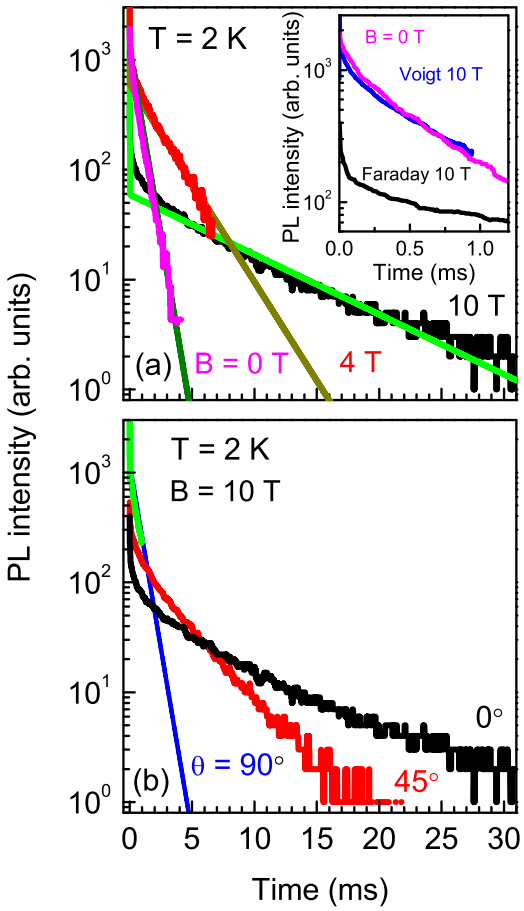

FIG. 7. PL dynamics of the LO_{AlAs} line measured at $T = 2$ K. (a) In different longitudinal magnetic fields. Solid lines are model calculations with the parameters given in text. Inset shows the dynamics of the LO_{AlAs} line at $B = 0$ T (magenta) and 10 T in the Faraday (black) and Voigt geometries (blue). (b) At $B = 10$ T for various angles θ.

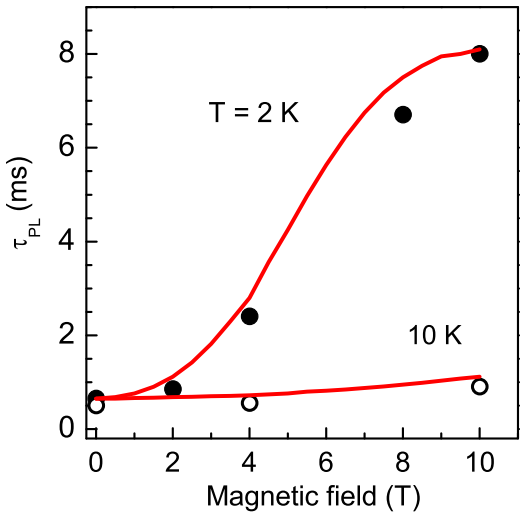

FIG. 8. PL decay of the LO_{AlAs} line measured at $T = 2$ K (full circles) and 10 K (open circles) as a function of longitudinal magnetic field. Red lines show results of modeling with the parameters given in the text.

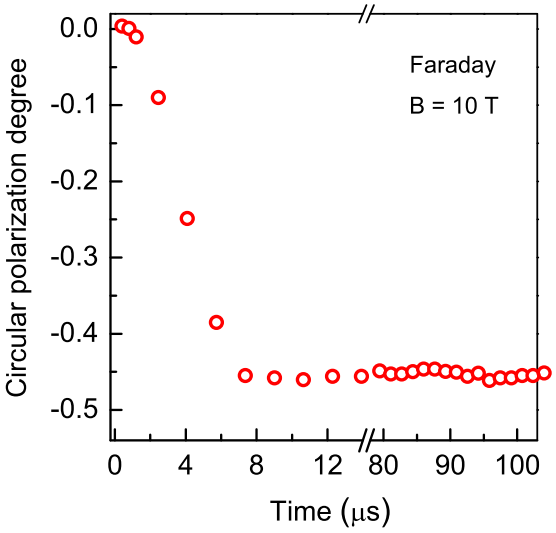

FIG. 9. Dynamics of the circular polarization degree of the LO_{AlAs} emission line measured at $T = 2$ K and $B = 10$ T in the Faraday geometry.

and temperature dependencies we need information on the relative time scales of the spin and recombination dynamics in the studied sample. For that we measured the PL dynamics in the Faraday geometry at $B = 10$ T for the two circular polarized components, i.e., $I_{PL}(\sigma^+)$ and $I_{PL}(\sigma^-)$, and plot in Fig. 9 the dynamics of the circular polarization degree $P_c(t) = [I_{PL}(\sigma^+) - I_{PL}(\sigma^-)]/[I_{PL}(\sigma^+) + I_{PL}(\sigma^-)]$. Circular polarization is absent for short delay times, then decreases and saturates at about -45% within a characteristic time τ_s of about 4 μs, which is much shorter than the recombination decay of the long-term component.

In conclusion of this section, we summarize the most important experimental findings: (i) The intensity and dynamics of the exciton radiative recombination depend strongly on the magnetic field strength in the Faraday and tilted-field geometries. This effect is absent in the Voigt geometry. Therefore it is induced by the magnetic field component parallel to the z axis. (ii) A quite small temperature increase destroys the effect of the magnetic field on the exciton PL intensity and decay times. Thus, one can conclude that nonradiative recombination plays an important role for the exciton recombination dynamics in thin GaAs/AlAs QWs. Changes of the temperature or longitudinal component of the magnetic field can drastically affect the exciton redistribution between the radiative and nonradiative recombination channels.

IV. THEORY

A. Exciton fine structure in the magnetic field

In the ultrathin GaAs/AlAs QW structure under study the indirect exciton is formed by a Γ-point heavy hole in the GaAs layer and an electron in the X_x or X_y valley of the AlAs layer. The corresponding band diagram for the indirect band gap structures with a type-II band alignment is shown schematically in Fig. 1(f); see also Refs. [5,20–22] for details. In order to simplify the further analysis we consider the conduction band states in one of the valleys $X_{x,y}$ since the

inclusion of the other valley into the consideration does not change the result. The exciton states $|s,j\rangle$ are labeled by the two spin indices, $s = \pm 1/2$ for the electron and $j = \pm 3/2$ for the heavy-hole spin states.

In the indirect excitons the electron-hole exchange interaction is suppressed [23] and the spin Hamiltonian of the electron-hole pair in the presence of an external magnetic field, **B**, contains only the Zeeman terms

$$\hat{\mathcal{H}} = g_e \mu_B \mathbf{B} \cdot \hat{\mathbf{s}} + \frac{g_{hh}}{3} \mu_B B_z \hat{J}_z. \tag{1}$$

Here μ_B is the Bohr magneton, g_e and g_{hh} are the electron and heavy-hole g factors, $\hat{\mathbf{s}}$ is the electron spin operator, and $\hat{J}_s$ is the operator of the heavy-hole angular-momentum z component. The heavy holes have a strongly anisotropic g factor and their in-plane component is disregarded [24]. The factor $1/3$ in the second term of Eq. (1) is introduced to have similar forms

$$\Delta_e = |g_e \mu_B \boldsymbol{B}|, \; \Delta_{hh} = |g_{hh} \mu_B B_z| \tag{2}$$

for the electron and heavy-hole Zeeman splittings. For convenience we will consider separately (i) the Faraday geometry, $\mathbf{B} \parallel z$, and (ii) the Voigt geometry, $\mathbf{B} \perp z$. The case of an arbitrary magnetic-field direction is briefly discussed at the end of this section.

We begin the analysis with the Faraday geometry. As illustrated in Fig. 10, the magnetic field fully lifts the level degeneracy and splits the exciton quadruplet $|s = \pm 1/2, j = \pm 3/2\rangle$ into four nondegenerate sublevels with energies $E(s,j)$ that are given, in accordance with Eq. (1), by

$$E(1/2,3/2) = \tfrac{1}{2}(g_e + g_{hh})\mu_B B_z, \tag{3a}$$

$$E(-1/2,3/2) = \tfrac{1}{2}(-g_e + g_{hh})\mu_B B_z, \tag{3b}$$

$$E(1/2,-3/2) = \tfrac{1}{2}(g_e - g_{hh})\mu_B B_z, \tag{3c}$$

$$E(-1/2,-3/2) = \tfrac{1}{2}(-g_e - g_{hh})\mu_B B_z. \tag{3d}$$

The energies are reckoned relative to the exciton energy at $B = 0$. The order of energy states is determined by the signs and relative values of the electron and hole g factors. Particularly, for $g_e > 0$, $g_{hh} > 0$, and $g_{hh} > g_e$ one has $g_e + g_{hh} > |g_e - g_{hh}|$ and the sublevels with $s + j = \pm 2$ have the highest and lowest energies, respectively; see Fig. 10(a). On the other hand, for $g_e > 0$, $g_{hh} < 0$, and $|g_{hh}| > g_e$ the relation $|g_e + g_{hh}| < |g_e - g_{hh}|$ holds and the uppermost and lowermost are the sublevels with $s + j = \mp 1$, Fig. 10(b).

The PL intensity is determined by the relative energy positions of the exciton sublevels, Eqs. (3), as well as by the interplay of the exciton radiative and nonradiative recombination channels. The radiative recombination occurs mainly through the phonon-assisted optical transitions; see Refs. [5,20–22,25]. Moreover, it is commonly accepted that the dominant contribution to the optical matrix element comes from a phonon-induced virtual transition of the electron from the X_{xy} to the Γ valley [22,25]. Neglecting effects of the spin-orbit coupling and the external magnetic field on the electron-phonon interaction matrix element (the general analysis can be carried out following Refs. [26,27]), we arrive at the following spin selection rules for the indirect exciton radiative recombination:

$$|s = -1/2, j = 3/2\rangle \text{ is active in } \sigma^+, \tag{4a}$$

$$|s = 1/2, j = -3/2\rangle \text{ is active in } \sigma^-, \tag{4b}$$

$$|s,j\rangle \text{ with } |s + j| = 2 \text{ are dark.} \tag{4c}$$

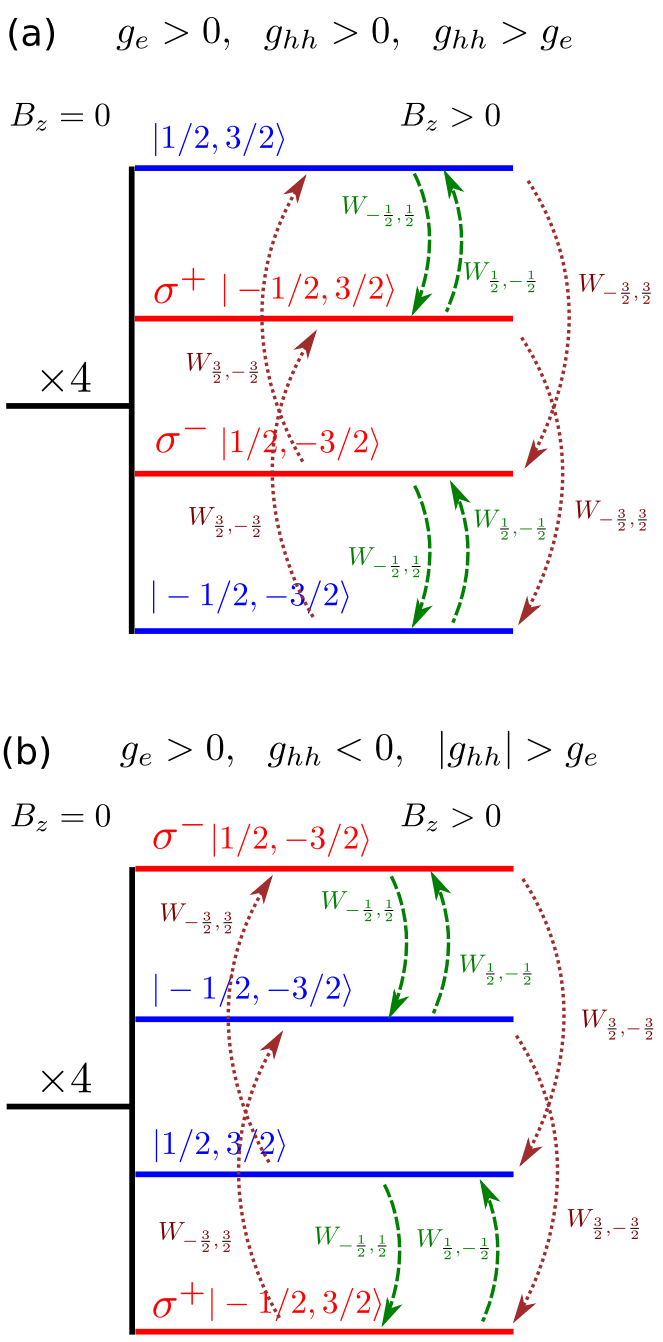

FIG. 10. Schematic illustration of the indirect-exciton spin levels in the Faraday geometry $\mathbf{B} \parallel z$. Blue lines show optically dark (spin-forbidden) states, red lines show spin-allowed bright states active in the σ^+ and σ^- polarizations. Dashed/green (dotted/brown) arrows demonstrate electron (hole) spin-flip processes. The energies are referred to the exciton quadruplet center energy at $B = 0$. Two cases are presented: (a) positive g_e, g_{hh} with $g_{hh} > g_e$, and (b) $g_e > 0$, $g_{hh} < 0$ with $|g_{hh}| > g_e$.

They readily follow from the selection rules for the direct Γ point optical transitions involving the heavy holes, as shown in Fig. 10 by the red lines. The nonradiative processes may involve recombination, e.g., via deep traps for which the spin selection rules are relaxed.

In order to model the PL kinetics one has to find the occupancies, f_{sj}, of the exciton states $|s,j\rangle$. These occupancies are governed by a set of kinetic equations in the form

$$\frac{df_{sj}}{dt} + (W_{\bar{s},s} + W_{\bar{j},j})f_{sj} - W_{s,\bar{s}}f_{\bar{s}j} - W_{j,\bar{j}}f_{s\bar{j}} + \left(\frac{1}{\tau_r}\delta_{|s+j|,1} + \frac{1}{\tau_{nr}}\right)f_{sj} = \gamma_{sj}(t). \quad (5)$$

Here $\bar{s} = -s$, $\bar{j} = -j$, $W_{s,s'}$ ($W_{j,j'}$) are the electron (heavy-hole) spin-flip rates for the transitions $s' \to s$ ($j' \to j$); τ_{nr} and τ_r are the nonradiative and radiative recombination times of excitons; the Kronecker δ symbol is defined as $\delta_{ab} = 1$ for $a = b$ and $\delta_{ab} = 0$ otherwise; and $\gamma_{sj}(t)$ is the exciton generation rate into the state $|s,j\rangle$. In deriving Eq. (5) we took into account the selection rules (4) and assumed the nonradiative recombination time to be the same for all the exciton states. Therefore, the dark states decay either nonradiatively or go over to the bright states via an electron or hole spin-flip. For an equilibrium phonon thermal bath, the ratio of the rates for processes with emission and absorption of a phonon is given by the Boltzmann exponent as follows:

$$W_{1/2,-1/2} = W_{-1/2,1/2}\exp\left(-\frac{g_e\mu_B B_z}{k_B T}\right), \quad (6a)$$

$$W_{3/2,-3/2} = W_{-3/2,3/2}\exp\left(-\frac{g_{hh}\mu_B B_z}{k_B T}\right), \quad (6b)$$

with T being the temperature and k_B being the Boltzmann constant. Moreover, for convenience, we define the electron and hole spin relaxation times

$$\tau_{s,e} = \frac{1}{2W_{\bar{s},s}}, \quad \tau_{s,hh} = \frac{1}{2W_{\bar{j},j}}, \quad (7)$$

where $W_{\bar{s},s}, W_{\bar{j},j}$ are the rates of flip-flop from the higher to the lower spin sublevels with s (j) being $+1/2$ ($+3/2$) for positive g_e (g_{hh}) and $-1/2$ ($-3/2$) for negative g_e (g_{hh}). Note that $\tau_{s,e}$ and $\tau_{s,hh}$ can depend, in general, on temperature and magnetic field strength. However, these dependencies are governed by power laws in contrast to the strong exponential factors in Eqs. (6); see Refs. [8,28–30] for details. For simplicity, in what follows $\tau_{s,e}$ and $\tau_{s,hh}$ are considered as fitting parameters, and their possible dependencies on magnetic field or temperature are neglected.

Under the assumptions outlined above, the intensities of the indirect exciton phonon replicas in the right (σ^+) and left (σ^-) circular polarizations are given by

$$I_\pm \propto \tau_r^{-1}\sum_{sj} f_{sj}\delta_{s+j,\pm 1}, \quad (8)$$

where f_{sj} are obtained from Eq. (5). Under the nonresonant excitation the photoexcited electrons and holes lose their spin orientation in the process of thermalization towards the exciton states $|s,j\rangle$. Therefore, γ_{sj} on the right-hand side of Eq. (5) should be set the same for all values of s and j, $\gamma_{sj} = G(t)$, with $G(t)$ being a function of time that is determined by the excitation conditions. Equation (8) holds both for pulsed and continuous-wave (cw) excitation. In the former case, for a short pulse one may solve Eq. (5) with $G(t) \propto \delta(t)$, while in the latter case G is a time-independent variable. Note that Eq. (5) is linear; hence the PL intensity under cw excitation and the time-integrated intensity under pulsed excitation differ by a common factor only.

Now we turn to the Voigt geometry ($\mathbf{B} \perp z$). In this case the hole spin states are not affected at all by the magnetic field, while the electron spin states $1/2$ and $-1/2$ get mixed. As a result, the quadruplet is split into two degenerate doublets with degeneracy index $j = \pm 3/2$ and energies

$$E_{1,2} = \pm\tfrac{1}{2}g_e\mu_B|\boldsymbol{B}|. \quad (9)$$

All four exciton states are optically active and, moreover, have the same oscillator strength since the electron wave function is a superposition of the $|s = 1/2\rangle$ and $|s = -1/2\rangle$ basic states having the same weights.

For an arbitrary orientation of the magnetic field, the degeneracy of the doublets (9) is lifted due to the splitting of the heavy-hole states induced by the B_z component. Moreover, the weights of the $|s = 1/2\rangle$ and $|s = -1/2\rangle$ contributions to the electron-in-exciton wave function are no longer equal. Hence, among the four exciton states two have higher oscillator strength and two have lower oscillator strength. The latter become dark for $\mathbf{B} \parallel z$.

B. Magnetic field effect on recombination dynamics of indirect excitons

The outlined model provides an interpretation of the main experimental findings under the following assumptions: (i) $g_e > 0$, $g_{hh} > 0$, $g_{hh} > g_e$; and (ii) the nonradiative processes are weak as compared with the radiative ones, $\tau_r \ll \tau_{nr}$. In this case, as shown in Fig. 10(a), for the magnetic field applied in the Faraday geometry the ground exciton state is spin-forbidden and, hence, dark. Therefore, application of the magnetic field results in preferential thermal occupation of the dark ground state at low temperatures and leads to quenching of the PL intensity. Note that such quenching is possible only in the presence of nonradiative recombination channels. Moreover, since the nonradiative channel of recombination is less effective compared with the radiative recombination of the bright states an increase in magnetic field slows down the PL decay: a dark exciton, before emission, needs to be converted to a bright one, which is a process that is suppressed by the field due to the exponential factors in Eqs. (6), which describe the decrease of the occupation number of phonons able to transfer an exciton from the ground (dark) state into one of the excited (bright) states. An increase in temperature causes an increase in the occupation of the bright states and, hence, restores the PL intensity and decay rate.

The scenario is expected to be quite different for the opposite signs of the g factors, $g_e > 0$, $g_{hh} < 0$, and $|g_{hh}|$ exceeding g_e, as shown in Fig. 10(b), in which case the exciton ground state is bright. Here an increase in the field does not seem to result in a significant variation of the PL intensity and exciton dynamics. Thus, analysis of the magnetic-field-dependent changes of PL intensity allows one to determine

details of the exciton fine structure. Note that weak magnetic-field dependencies also occur when the nonradiative processes become dominant, $\tau_r \gg \tau_{nr}$.

In the Voigt geometry all four exciton states are optically accessible and, hence, the magnetic field leaves the PL intensity and decay times practically unaffected, even for the case of Fig. 10(a): at high enough magnetic fields so that $|g_e|\mu_B B$ and $|g_{hh}|\mu_B B$ exceed the thermal energy $k_B T$ and the emission is almost fully quenched in the Faraday geometry, the dependence of the PL intensity on the angle θ between **B** and z should approximately follow a $\sin^2\theta$ law; see the inset in Fig. 4(b).

V. DISCUSSION

According to the model developed in Sec. IV the exciton recombination dynamics in a magnetic field is governed by

(1) the fine structure of the exciton states split by the magnetic field, and the splittings determined by the magnitudes and signs of the electron and heavy-hole g factors,

(2) the recombination times of bright and dark exciton states,

(3) the spin relaxation times for the electron and the heavy hole forming the exciton.

The model has a fair number of parameters. Therefore it is important to prove stability of the fitting. Let us demonstrate that very few of these variable parameters are required to describe our experimental data. Due to the large band gap at the X point, the spin-orbit contribution to the electron g factor is vanishingly small [15,31,32]. As a result, the electron g factor, g_e, is isotropic and its value almost coincides with the free-electron Landé factor of $+2.0$ [33]. On the other hand, the value of the hole g factor is determined by mixing of heavy and light holes, thus is very sensitive to the QW thickness and interface roughness and could be large and positive [34,35,36].

The electron and hole spin relaxation times, $\tau_{s,e}$ and $\tau_{s,hh}$, can be estimated from the dynamics of the PL circular polarization in Fig. 9. The characteristic time $\tau_s = 4$ μs of this dynamics gives an upper limit for the $\tau_{s,e}$ and $\tau_{s,hh}$ values; τ_s is by several orders of magnitude shorter than the PL decay time at any experimental conditions. Therefore, we can set $\tau_{s,e} = \tau_{s,hh} = \tau_s$, since possible changes of these parameters with increasing temperature and magnetic field strength cannot be detected in our experiment.

Thus, we have only three variable parameters: the recombination times of the bright and dark excitons and the value of the heavy-hole g factor which is positive and, according to the magnetic-field-induced circular-polarization sign, should exceed $+2$ [33]. The best fits to the PL intensity and PL decay at different temperatures and magnetic field strengths in the Faraday geometry are shown by curves in Figs. 7(a), 8, and 11 and are obtained with the following parameters: $\tau_r = 0.34$ ms for the bright-exciton radiative recombination, $\tau_{nr} = 8.5$ ms for the nonradiative recombination of both the dark and the bright states, and $g_{hh} \geqslant +2.5$ for the heavy-hole longitudinal g factor. A small deviation of $\sim$10% only in the values of τ_r and τ_{nr} ruins already the agreement with the experimental PL dynamics within the studied range of magnetic field strengths. In contrast, variation of g_{hh} in the range 2.5...10 results in small deviations of the fitting curve from the experimental data, which reflects the fact that the Zeeman splitting between the lowest levels of the bright and dark excitons is independent of the heavy-hole longitudinal g factor.

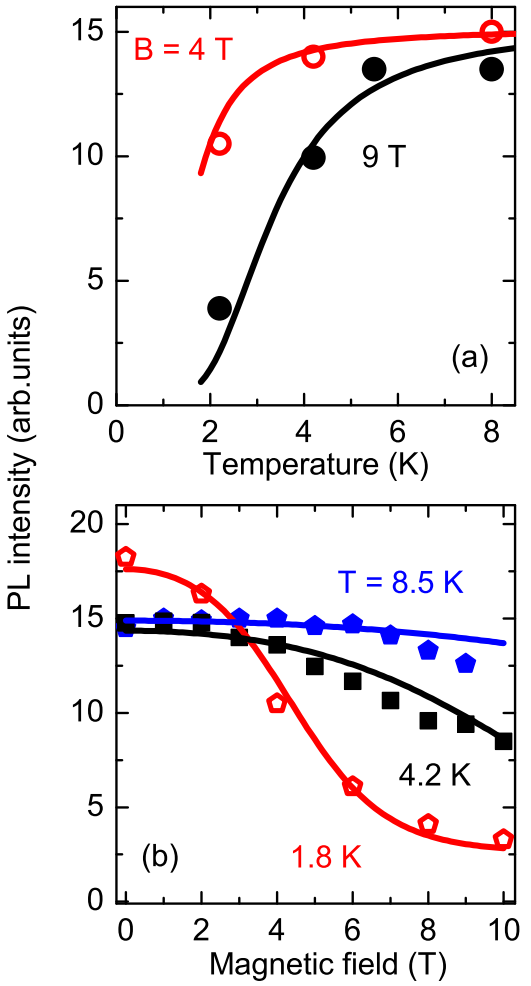

FIG. 11. Fitting of the (a) temperature dependence of the PL intensity measured at longitudinal magnetic fields $B = 4$ T and 9 T with the parameters given in the text and (b) longitudinal magnetic field dependence of the PL intensity measured at $T = 1.8$,4.2, and 8.5 K.

One can see from the curves in Figs. 7(a) and 8 and the time-integrated PL data in Fig. 11 that the model reproduces in detail the exciton dynamics in the Faraday geometry. The small deviation between calculation and experiment for higher temperatures ($T > 8$ K) can be ascribed to an increase of the nonradiative recombination rate which is ignored in the model. It is worth mentioning that to achieve a better fit in Fig. 11(b) a constant, magnetic-field-independent offset (about 10% of the zero-field PL intensity) has been added to the theoretical curves. Its origin is not fully clear; it could be related with a weak magnetic-field-induced variation of the radiative and/or nonradiative decay rates and an emergence of a decay channel for dark excitons in strong magnetic fields, e.g., excitons localized at low-symmetry sites.

VI. CONCLUSION

The recombination dynamics of excitons indirect in real and $\boldsymbol{k}$ space and involving electrons from the $X_{x,y}$ valleys has been investigated experimentally in a two-monolayer-thick GaAs/AlAs quantum well. In this system an indirect band gap and a type-II band alignment are realized. In longitudinal magnetic fields and at low temperatures, when the Zeeman splitting of the exciton levels exceeds the thermal energy $k_B T$, relaxation from the bright to the dark exciton state results in a decrease of the exciton emission intensity which is accompanied by an increase of the exciton recombination time. A recovery of the recombination time and emission intensity is observed in the presence of a transverse component of the magnetic field which mixes the dark and bright exciton states and for a temperature increase resulting in thermal population of the bright states. The developed model provides a satisfactory description of the experimental data which allows us to evaluate the heavy-hole longitudinal g factor, $g_{hh} \geqslant +2.5$, the radiative recombination time for the bright excitons (0.34 ms), and the nonradiative recombination time of bright and dark excitons (8.5 ms).

ACKNOWLEDGMENTS

This work was supported by the German Ministry of Education and Research (BMBF) (FKZ: 05K13PE1), the Deutsche Forschungsgemeinschaft and the Russian Foundation for Basic Research via ICRC TRR160, the Russian Foundation for Basic Research (Grants No. 16-02-00242, No. 15-52-12012, and No. 14-02-00033), Russian Federation Government Grant No. 14.Z50.31.0021 (leading scientist M. Bayer), and by Act 211 Government of the Russian Federation (Contract No. 02.A03.21.0006).

[1] *Optics of Semiconductors and Their Nanostructures*, edited by H. Kalt and M. Hetterich (Springer-Verlag, Berlin, 2004).

[2] C. F. Klingshirn, *Semiconductor Optics* (Springer-Verlag, Heidelberg, 2012).

[3] R. Cingolani and K. Ploog, Frequency and density dependent radiative recombination processes in III-V semiconductor quantum wells and superlattices, Adv. Phys. **40**, 535 (1991).

[4] F. Hatami, M. Grundmann, N. N. Ledentsov, F. Heinrichsdorff, R. Heitz, J. Böhrer, D. Bimberg, S. S. Ruvimov, P. Werner, V. M. Ustinov, P. S. Kop'ev, and Zh. I. Alferov, Carrier dynamics in type-II GaSb/GaAs quantum dots, Phys. Rev. B **57**, 4635 (1998).

[5] T. S. Shamirzaev, A. M. Gilinsky, A. K. Kalagin, A. V. Nenashev, and K. S. Zhuravlev, Energy spectrum and structure of thin pseudomorphic InAs quantum wells in an AlAs matrix: Photoluminescence spectra and band-structure calculations, Phys. Rev. B **76**, 155309 (2007).

[6] L. P. Fu, F. T. Bacalzo, G. D. Gilliland, R. Chen, K. K. Bajaj, J. Klem, and D. J. Wolford, Microscopic mechanisms governing exciton-decay kinetics in type-II GaAs/AlAs superlattices, Phys. Rev. B **52**, 2682 (1995).

[7] A. V. Khaetskii and Yu. V. Nazarov, Spin relaxation in semiconductor quantum dots, Phys. Rev. B **61**, 12639 (2000).

[8] A. V. Khaetskii, and Y. V. Nazarov, Spin-flip transitions between Zeeman sublevels in semiconductor quantum dots, Phys. Rev. B **64**, 125316 (2001).

[9] W. A. J. A. van der Poel, A. L. G. J. Severens, H. W. van Kesteren, and C. T. Foxon, Spin relaxation in type-II GaAs/AlAs quantum wells, Phys. Rev. B **39**, 8552 (1989).

[10] S. Sasaki and N. Miura, High-field magneto-optical study of type II GaAs/AlAs short-period superlattices, Appl. Phys. Lett. **59**, 96 (1991).

[11] C. Gourdon and P. Lavallard, Fine structure of heavy excitons in GaAs/AlAs superlattices, Phys. Rev. B **46**, 4644 (1992).

[12] P. G. Baranov, N. G. Romanov, A. Hofstaetter, A. Scharmann, C. Schnorr, F.-J. Ahlers, and K. Pierz, Exchange interactions of excitons localized at opposite interfaces in type-II GaAs/AlAs superlattices: Optically detected magnetic resonance and level anticrossing, JETP Lett. **64**, 754 (1996).

[13] R. I. Dzhioev, H. M. Gibbs, E. L. Ivchenko, G. Khitrova, V. L. Korenev, M. N. Tkachuk, and B. P. Zakharchenya, Determination of interface preference by observation of linear-to-circular polarization conversion under optical orientation of excitons in type-II GaAs/AlAs superlattices, Phys. Rev. B **56**, 13405 (1997).

[14] I. V. Mashkov, C. Gourdon, P. Lavallard, and D. Yu. Roditchev, Exciton quantum beats in type-II GaAs/AlAs superlattices in longitudinal and in-plane magnetic fields, Phys. Rev. B **55**, 13761 (1997).

[15] E. L. Ivchenko, *Optical Spectroscopy of Semiconductor Nanostructures* (Alpha Science, Harrow, UK, 2005).

[16] We choose for this study very thin GaAs QWs in order to be able to compare their properties with another model InAs/AlAs QW structure, which has indirect band gap, but a type-I band alignment. Due to strain, high quality InAs/AlAs QWs can be grown of only a few monolayer thicknesses. This is not a crucial limitation for GaAs/AlAs heteropairs; these QWs can be grown with larger thicknesses.

[17] T. S. Shamirzaev, J. Debus, D. S. Abramkin, D. Dunker, D. R. Yakovlev, D. V. Dmitriev, A. K. Gutakovskii, L. S. Braginsky, K. S. Zhuravlev, and M. Bayer, Exciton recombination dynamics in an ensemble of (In, Al)As/AlAs quantum dots with indirect band-gap and type-I band alignment, Phys. Rev. B **84**, 155318 (2011).

[18] *Physics of Group IV Elements and III-V Compounds*, edited by O. Madelung, M. Schulz, and H. Weiss, Landolt-Börnstein Numerical Data and Relationships, New Series, Group III, Vol. 17, Pt. A (Springer, Berlin, 1982).

[19] I. N. Krivorotov, T. Chang, G. D. Gilliland, L. P. Fu, K. K. Bajaj, and D. J. Wolford, Exciton transport and nonradiative decay in semiconductor nanostructures, Phys. Rev. B **58**, 10687 (1998).

[20] D. Scalbert, J. Cernogora, C. Benoit á la Guillaume, M. Maaref, F. F. Charfi, and R. Planel, Nature of the lowest electron states in short period GaAs/AlAs superlattices of type II, Solid State Commun. **70**, 945 (1989).

[21] P. Dawson, C. T. Foxon, and H. W. van Kesteren, Nature of the lowest confined electron state in GaAs/AlAs type II quantum

wells as a function of AlAs thickness, Semicond. Sci. Technol. **5**, 54 (1990).

[22] M. Maaref, F. F. Charfi, D. Scalbert, C. Benoit á la Guillaume, and R. Planel, Recombination processes in short-period GaAs-AlAs superlattices of type II, Phys. Status Solidi B **170**, 637 (1992).

[23] G. E. Pikus and G. L. Bir, Exchange interaction in excitons in semiconductors, Sov. Phys. JETP **33**, 108 (1971) [Zh. Eksp. Teor. Fiz. **60**, 195 (1971)].

[24] X. Marie, T. Amand, P. Le Jeune, M. Paillard, P. Renucci, L. E. Golub, V. D. Dymnikov, and E. L. Ivchenko, Hole spin quantum beats in quantum-well structures, Phys. Rev. B **60**, 5811 (1999).

[25] P. Dawson, K. J. Moore, C. T. Foxon, G. W. 't Hooft, and R. P. M. van Hal, Photoluminescence decay time studies of type II GaAs/AlAs quantum well structures, J. Appl. Phys. **65**, 3606 (1989).

[26] V. M. Asnin, G. L. Bir, Yu. N. Lomasov, G. E. Pikus, and A. A. Rogachev, Polarization of exciton luminescence in an external magnetic field, Sov. Phys. JETP **44**, 838 (1976) [Zh. Eksp. Teor. Fiz. **71**, 1600 (1976)].

[27] Z. Liu, M. O. Nestoklon, J. L. Cheng, E. L. Ivchenko, and M. W. Wu, Spin-dependent intravalley and intervalley electron-phonon scatterings in germanium, Phys. Solid State **55**, 1619 (2013).

[28] D. Pines, J. Bardeen, and C. P. Slichter, Nuclear polarization and impurity-state spin relaxation processes in silicon, Phys. Rev. **106**, 489 (1957).

[29] L. M. Woods, T. L. Reinecke, and Y. Lyanda-Geller, Spin relaxation in quantum dots, Phys. Rev. B **66**, 161318 (2002).

[30] F. Marquardt and V. A. Abalmassov, Spin relaxation in a quantum dot due to Nyquist noise, Phys. Rev. B **71**, 165325 (2005).

[31] I. A. Yugova, A. Greilich, D. R. Yakovlev, A. A. Kiselev, M. Bayer, V. V. Petrov, Yu. K. Dolgikh, D. Reuter, and A. D. Wieck, Universal behavior of the electron g factor in GaAs/$Al_xGa_{1-x}As$ quantum wells, Phys. Rev. B **75**, 245302 (2007).

[32] I. Vurgaftman, J. R. Meyer, and L. R. Ram-Mohan, Band parameters for III-V compound semiconductors and their alloys, J. Appl. Phys. **89**, 5815 (2001).

[33] J. Debus, T. S. Shamirzaev, D. Dunker, V. F. Sapega, E. L. Ivchenko, D. R. Yakovlev, A. I. Toropov, and M. Bayer, Spin-flip Raman scattering of the Γ-X mixed exciton in indirect band gap (In, Al)As/AlAs quantum dots, Phys. Rev. B **90**, 125431 (2014).

[34] G. E. Pikus and F. G. Pikus, The mechanism of heavy and light hole mixing in GaAs/AIAs superlattices, Solid State Commun. **89**, 319 (1994).

[35] A. A. Kiselev and L. V. Moiseev, Zeeman splitting of heavy-hole states in III-V and II-VI heterostructures, Phys. Solid State **38**, 866 (1996).

[36] D. M. Hofmann, K. Oettinger, Al. L. Efros, and B. K. Meyer, Magnetic-circular-dichroism study of heavy- and light-hole g factors in $In_xGa_{1-x}As$/InP quantum wells, Phys. Rev. B **55**, 9924 (1997).